Supporting Information for "Oceanic mesoscale eddy depletion catalyzed by internal waves"

Roy Barkan[1,2], Kaushik Srinivasan[2], Luwei Yang[2], James C. McWilliams[2],

Jonathan Gula[3,4], Clément Vic[3]

[1]Porter School of the Environment and Earth Sciences, Tel Aviv University, Ramat Aviv, Israel 6997801

[2]Department of Atmospheric and Oceanic Sciences, University of California, Los Angeles, CA 90095

[3]Laboratoire d'Océanographie Physique et Spatiale, Université de Bretagne Occidentale, Plouzané, France 29280

[4]Institut Universitaire de France (IUF)

Contents of this file

1. Text S1 to S3

2. Figures S1 to S6

3. Tables S1

————

Corresponding author: R. Barkan, Porter School of the Environment and Earth Sciences, Tel Aviv University, Ramat Aviv, Israel 6997801, and Department of Atmospheric and Oceanic Sciences, University of California, Los Angeles, CA 90095, USA. (rbarkan@tauex.tau.ac.il)

May 16, 2021, 2:46pm

Introduction

The supporting information provides details about the modeling approach and setup, including the required parameters to reproduce the numerical solutions described in the manuscript. In addition, it provides detailed information about the various data sets and analysis methods used to compare between model solutions and *in-situ* measurements. Finally, it provides additional figures and discussion to complement and support the energetic analysis shown in the main manuscript.

S1: Modelling

All simulations are carried out using the Regional Oceanic Modeling System (ROMS; Shchepetkin & McWilliams, 2005), which solves the Primitive Equations in terrain following coordinates using the full equation of state for seawater (Shchepetkin & McWilliams, 2011). We utilize a one-way nesting procedure as described in Mason et al. (2010) with successive, nearly isotropic ($dx \approx dy$) grid resolutions, varying from $\approx$ 6 km covering most of the Atlantic Ocean, $\approx$ 2 km for the North Atlantic Subpolar Gyre region, and $\approx$ 500 m for the Iceland basin (Figure 1a). The stretching parameters for all simulations are H_{cline}=350m, $\theta_s = 6$, $\theta_b = 4.5$. The number of sigma levels used is 50, 100, and 150 for the 6 km, 2km, and 500 m nests, respectively. For the 2 km (500 m) solution analyzed in this manuscript, assuming a water depth of 3 km, the above parameters correspond to vertical resolution of approximately 3 m (2 m) near the surface, which gradually decays down to approximately 26 m (17 m) at 500 m depth. The bathymetry for all domains is constructed from the SRTM30_PLUS dataset (available at http://topex.ucsd.edu/WWW_html/srtm30_plus.html) and is smoothed to avoid aliasing

whenever the bathymetric data are available at higher resolution than the computation grid (e.g. Lemarié et al., 2012). The boundary conditions for the outermost nest are from the Simple Ocean Data Assimilation (SODA; Carton & Giese, 2008), and atmospheric forcing is from the Climate Forecast System Reanalysis (CFSR) atmospheric product (Dee et al., 2014) with hourly temporal resolution. The surface turbulent evaporation, heat, and momentum fluxes are estimated using bulk formulae (W. B. Large, 2006), and take into account ocean current feedback effects (e.g. Renault et al., 2016). TPXO-based (Egbert et al., 1994; Egbert & Erofeeva, 2002) barotropic tidal forcing is applied at the boundary of the 2 km nest. In the analyzed solutions the vertical mixing of tracers and momentum at the surface and bottom boundary layers is done with the K-profile parametrization (KPP) (W. G. Large et al., 1994). A third order horizontal upstream-biased advection scheme, which implicitly works as a horizontal mixing parametrization for momenta and tracers, is used and augmented by the vertical semi-implicit advection scheme discussed in Shchepetkin (2015). Solutions forced by both hourly winds, hourly boundary forcing, and barotropic tides are called high-frequency (HF). Solutions forced by hourly winds and hourly boundary forcing but without barotropic tidal forcing are called no-tides (NT). Solutions without barotropic tidal forcing and with smoothed wind and boundary forcing are called smooth (SM). The smoothing in the SM solutions for both the wind velocities at 10 m and the boundary files is carried out using a Gaussian low-pass filter with a filter width of 24 hours.

S2: Comparison with measurements

Power spectral densities comparison with Mooring data

The moorings used for comparison with the model's power spectral densities are the Irminger West (IRW), the Reykjanes Ridge Top (RRT), and the Iceland East (ICE), located at (33.259°W, 59.091°N), (30.669°W, 58.773°N), and (28.447°W, 57.58°N), respectively. They were deployed on 16 - 28 June 2015 and recovered on 23 - 28 July 2017 (see cruise reports Branellec & Thierry, 2016, 2018 for details on the operations), and were designed to investigate internal wave activity in the cross-ridge direction (Vic et al., 2021). The data used in this study are from Teledyne WorkHorse acoustic Doppler current profilers (ADCPs) and Aanderaa Doppler and Nortek Aquadopp current meters. The 75-kHz (150-kHz) ADCPs recorded horizontal velocity every 180 s (30 s) with 16 m (8 m) vertical bins, using a single ping per ensemble to save up energy for the long-term deployment. Aanderaa and Aquadopp current meters recorded velocity every 600 s and 3600 s, respectively. Data quality was overall good except for short-term periods when measurements done by the upward-looking ADCPs close to the surface were contaminated by surface wave-induced signals. Those data were flagged and discarded from the analysis. Data was linearly interpolated on the vertical on an 8-m grid.

Only the data at depths 150 m, 300 m, and 600 m are used for validation. The data below that depth are not used because we suspect that the model KE is not yet equilibrated below this depth. Because the majority of the interactions and KE differences are largely confined to the upper 200 m, we do not believe that this potential lack of equilibration below 600 m depth should affect the results presented in this manuscript.

The power spectral densities from the mooring data are averaged over the three moorings in each season. To increase the number of degrees of freedom each time series was divided into 5 segments with a 50% overlap. The shading in Figure 2 represents the 95% confidence interval based on 30 degrees of freedom. The exception is the power spectral densities for winter 2016, where only two moorings were used (20 degrees of freedom) due to some missing data. The temporal power spectral densities from the model solutions were computed for winter and summer months at every point in the domain occupied by the 500 m grid (Fig. 1a) and then spatially averaged.

Geostrophic eddy kinetic energy comparison with AVISO

The seasonal and annual geostrophic eddy kinetic energy in ROMS was computed from the sea-surface-height field of the 2 km HF solution, where 'eddy' is defined as the perturbation from an annual mean. In order to compare the model results to the Archiving, Validation, and Interpretation of Satellite Oceanographic Data (AVISO) dataset (Ducet et al., 2000), we computed the geostrophic eddy kinetic energy from the sea surface height of the model, which was smoothed using a spatial two-dimensional Gaussian low-pass filter with a filter width of 40 km, and a temporal low-pass Gaussian filter with a filter width of 1 week.

Stratification comparison with Argo

The Argo (Argo, 2000) stratification data was computed based on profiles collected during winter and summer months between 2005 and 2019. The stratification estimates were obtained from the 1×1 degree variational interpolated monthly mean (http://apdrc.soest.hawaii.edu/projects/Argo/data/gridded/On_standard_levels/index1.html).

The Argo climatology is based on the World Ocean Atlas inferred statistics that can be downloaded at https://www.seanoe.org/data/00612/72432/. Figure S1 shows a comparison between the Argo-based and the model-based stratification estimates for the 2 km and 500 m domains.

S3: Energetics

Mesoscale energy computation

Figures S2 and S3 display the depth structure of the horizontally-averaged low-passed mesoscale KE from the 2 km and 500 m solutions, respectively. For both solutions the spatial average is done over the region occupied by the 500 m domain (Fig. 1a) and a 6th order Butterworth filter with a 1 week filter width is used for low-passing. The numbers in the bottom left corner of each panel indicate the seasonal- and depth-averaged low-passed KE over the top 500 m, and are summarized in Table S1. We verified that the differences in the low-passed energies are not associated with differences in the seasonal-mean KE, which are an order of magnitude smaller than the values reported here (not shown). For the 2 km solution, if we spatially average over the entire domain and not only the region occupied by the 500 m grid (Table S1), the KE reductions in the HF solution become 24% and 38% for winter and summer, respectively. These regional variations in the low-passed KE suggest that the results reported in the manuscript, which focus on the 500 m grid, are rather conservative.

Wind-work computation

The wind forcing in the model solutions is applied using a bulk formula, and the implementation takes into account current feedback effects (see SI-Modeling). Therefore, we cannot filter the wind stresses directly and instead, to generate SM solutions without NIW forcing, we filter the atmospheric wind velocities at 10 m height. Consequently, it is important to verify that the changes in the low-passed KE shown in Figs. S2 and S3 are not because of the modifications to the wind forcing. To this end we compute the seasonally- and horizontally-averaged low-passed and high-passed wind work $\boldsymbol{u}_s^{\mathrm{LP}} \cdot \boldsymbol{\mathcal{T}}^{\mathrm{LP}}$ and $\boldsymbol{u}_s^{\mathrm{HP}} \cdot \boldsymbol{\mathcal{T}}^{\mathrm{HP}}$ (Fig. S4). Above, $\boldsymbol{u}_s$ is the horizontal velocity vector at the surface, $\boldsymbol{\mathcal{T}}$ is the surface wind stress vector, and LP and HP denote low-pass and high-pass filters, respectively, using a one week filter width. As shown in Fig. S4a,b, the low-passed wind work in the HF and SM solutions is quite similar during both seasons and, separately, between the 2 km and between the 500 m solutions. The differences between the 2 km and 500 m solutions (e.g., around day 25 in Fig. S4a) are a result of averaging over different domains. Quantitatively, there is more low-passed wind work in the HF solutions compared with the SM solutions, which is the opposite trend to that shown by the low-frequency KE values (Figs. S2 and S3, and Table S1). This shows that the reported reduction in low-passed KE cannot be explained by wind-work differences. The high-passed wind work (Fig. S4c,d) is displayed for completeness, and shows a substantial magnitude reduction in the SM solutions, as expected.

Cross-scale transfers in the 2 km solutions

Figure 3 (panels c-f) shows the depth structure of the spatially- and seasonally-averaged coarse-graining KE fluxes as a function of depth for the 500 m solutions. For completeness we show here the depth structure of the coarse-graining KE fluxes for the 2 km solutions (Fig. S5), where spatial averages are computed over the region occupied by the 500 m grid (Fig. 1a). Qualitatively, the signals are similar between the 500 m and 2 km solutions, however quantitatively the flux magnitudes are stronger in the 500 m solutions, particularly during winter. Similar patterns are found when the KE fluxes are computed over the entire 2 km domain (not shown), however the decrease in the inverse cascade magnitudes at low frequencies in the HF solution (compared with the SM solution) and the increase in the forward cascade magnitudes at super-inertial frequencies is larger when averages are taken over the entire 2 km domain. This explains why the integrated differences in the low-passed KE between the 2 km HF and SM solutions discussed above are larger when averaged over the entire 2 km domain.

Flow structures in the 500 m SM solution

Figure 4 quantifies the flow structures where the forward KE fluxes to super-inertial frequencies take place in the 500 m HF solution during winter. For completeness we show here the same analysis carried out for the 500 m SM solution during winter (Fig. S6). Similarly to the HF solution (Fig. 4c-e), Π_{14} in the SM solution is also enhanced at strong frontal features (Fig. S6c), which are again characterized by large magnitudes of cyclonic vorticity and convergence (Fig. S6d,e). Quantitatively however, the forward-flux magnitudes are generally weaker and shallower compared with the HF solution, in

agreement with Fig. 3. There are some differences in the RMS and skewness values of ζ/f and δ/f between the HF and SM solutions, but these may just be a result of different numerical iterations of turbulent flows and are not necessarily associated with internal wave effects. Finally, the pattern correlation between regions of strong and positive Π_{14} values and regions of strong fronts is not as high as in the HF solution (Fig. 4a,b and Fig. S6a,b). This suggests that the IW-induced forward fluxes are especially concentrated at fronts, compared with the more traditional forward fluxes that are associated with submesoscale currents.

References

Argo. (2000). Argo float data and metadata from global data assembly centre (argo gdac). *SEANOE*.

Branellec, P., & Thierry, V. (2016). Rrex 2015. ctd-o2 data report. *ODE/LOPS/16-26*.

Branellec, P., & Thierry, V. (2018). Rrex 2017. ctd-o2 data report. *Rap. Int. LOPS/18-04*.

Carton, J. A., & Giese, B. S. (2008). A reanalysis of ocean climate using simple ocean data assimilation (soda). *Monthly weather review*, *136*(8), 2999–3017.

Dee, D., Balmaseda, M., Balsamo, G., Engelen, R., Simmons, A., & Thépaut, J.-N. (2014). Toward a consistent reanalysis of the climate system. *Bulletin of the American Meteorological Society*, *95*(8), 1235–1248.

Ducet, N., Le Traon, P.-Y., & Reverdin, G. (2000). Global high-resolution mapping of ocean circulation from topex/poseidon and ers-1 and-2. *Journal of Geophysical Research: Oceans*, *105*(C8), 19477–19498.

Egbert, G. D., Bennett, A. F., & Foreman, M. G. (1994). Topex/poseidon tides estimated using a global inverse model. *Journal of Geophysical Research: Oceans*, *99*(C12), 24821–24852.

Egbert, G. D., & Erofeeva, S. Y. (2002). Efficient inverse modeling of barotropic ocean tides. *Journal of Atmospheric and Oceanic technology*, *19*(2), 183–204.

Large, W. B. (2006). Surface fluxes for practitioners of global ocean data assimilation. In *Ocean weather forecasting* (pp. 229–270). Springer.

Large, W. G., McWilliams, J. C., & Doney, S. C. (1994). Oceanic vertical mixing: A review and a model with a nonlocal boundary layer parameterization. *Rev. of Geophys.*, *32*, 363–403.

Lemarié, F., Kurian, J., Shchepetkin, A. F., Molemaker, M. J., Colas, F., & McWilliams, J. C. (2012). Are there inescapable issues prohibiting the use of terrain-following coordinates in climate models? *Ocean Modelling*, *42*, 57–79.

Mason, E., Molemaker, J., Shchepetkin, A. F., Colas, F., McWilliams, J. C., & Sangrà, P. (2010). Procedures for offline grid nesting in regional ocean models. *Ocean Modelling*,

35, 1–15.

Renault, L., Molemaker, M. J., McWilliams, J. C., Shchepetkin, A. F., Lemarié, F., Chelton, D., ... Hall, A. (2016). Modulation of wind work by oceanic current interaction with the atmosphere. *J. Phys. Oceanogr.*, *46*, 1685–1704.

Shchepetkin, A. F. (2015). An adaptive, courant-number-dependent implicit scheme for vertical advection in oceanic modeling. *Ocean Modelling*, *91*, 38–69.

Shchepetkin, A. F., & McWilliams, J. C. (2005). The Regional Oceanic Modeling System: A split-explicit, free-surface, topography-following-coordinate oceanic model. *Ocean Modelling*, *9*, 347–404.

Shchepetkin, A. F., & McWilliams, J. C. (2011). Accurate Boussinesq oceanic modeling with a practical, "stiffened" equation of state. *Ocean Modelling*, *38*, 41–70.

Vic, C., Ferron, B., Thierry, V., Mercier, H., & Lherminier, P. (2021). Tidal and near-inertial internal waves over the Reykjanes Ridge. *Journal of Physical Oceanography*, *51*(2), 419–437.
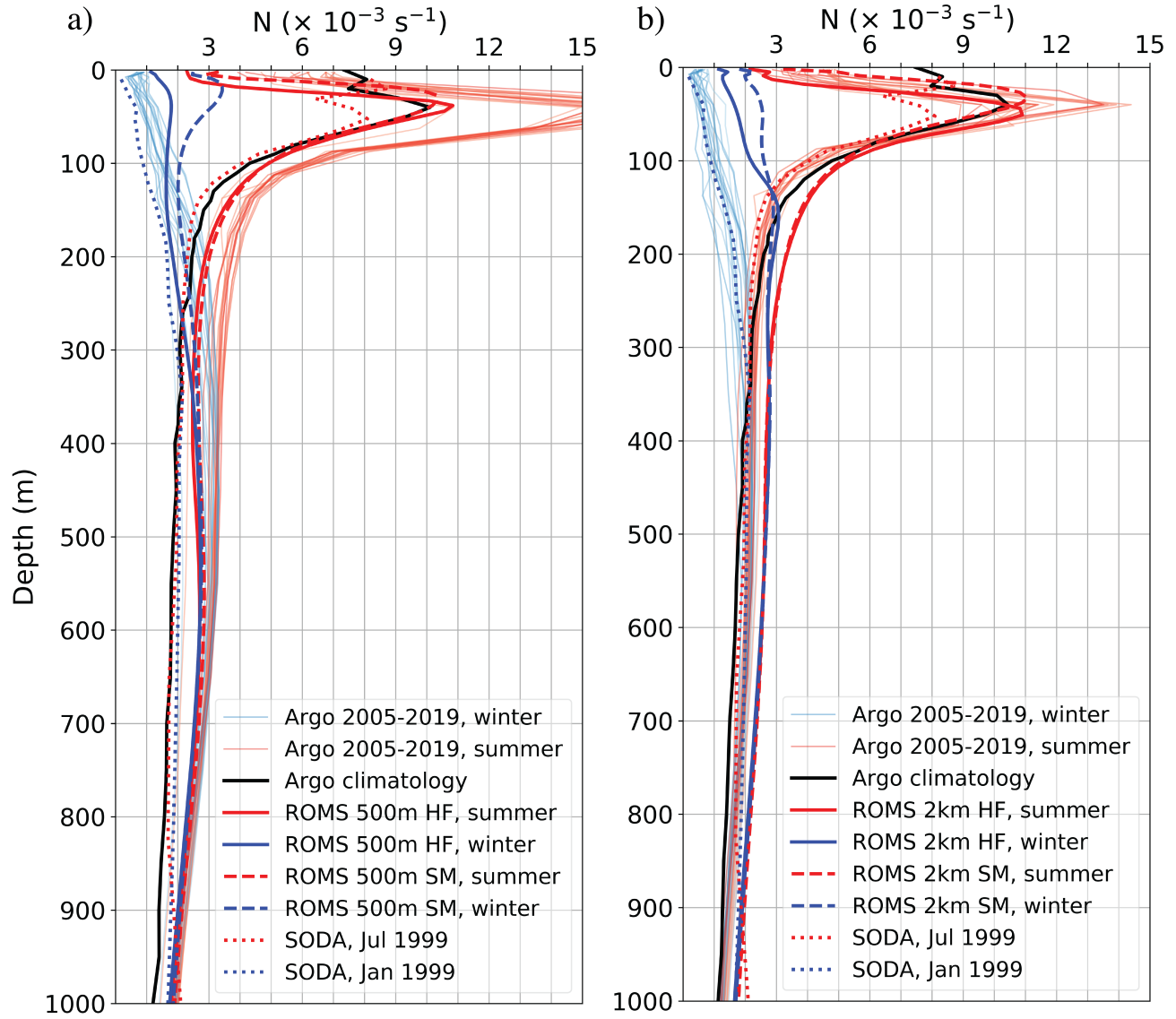
Figure S1: Same as Figure 1b for a) the 500 m solutions and b) the 2 km solutions.
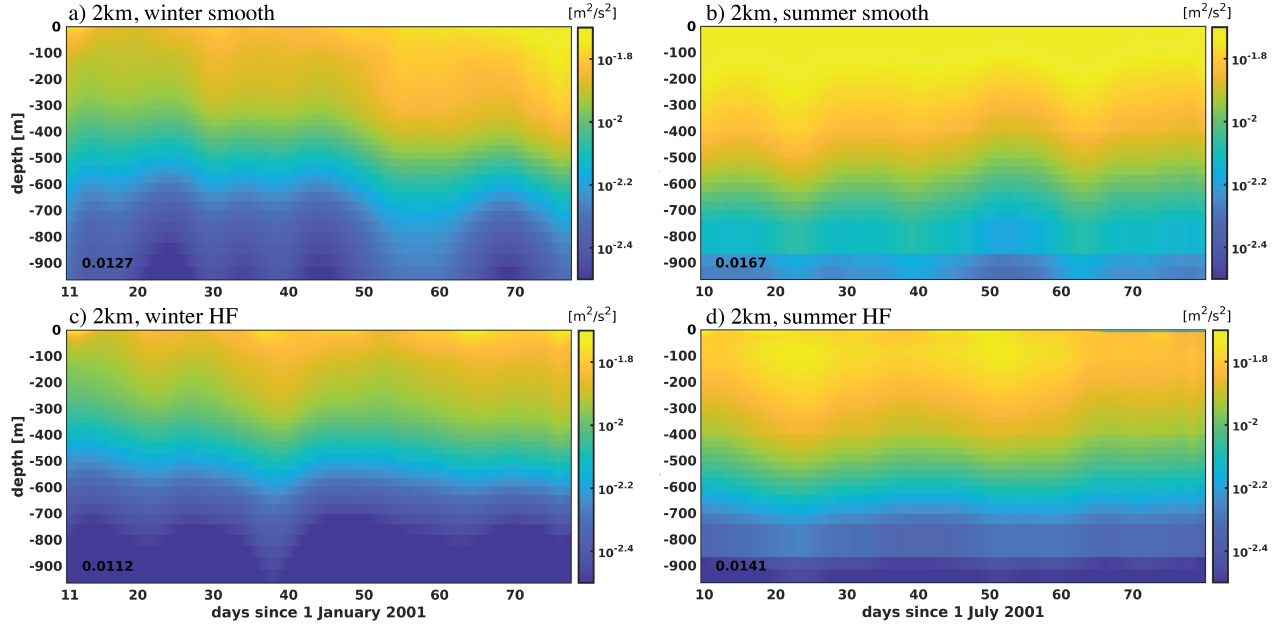
May 16, 2021, 2:46pm

Figure S2: The horizontally-averaged low-passed KE in the 2 km solutions. HF denotes solutions with IW forcing and SM denotes solutions without IW forcing. Spatial averages are taken over the domain occupied by the 500 m grid (Fig. 1a). A sixth order Butterworth filter with a one week filter width is used for low-passing. The values in the lower left corner of each panel indicate the seasonal- and depth-averaged KE over the top 500 m.
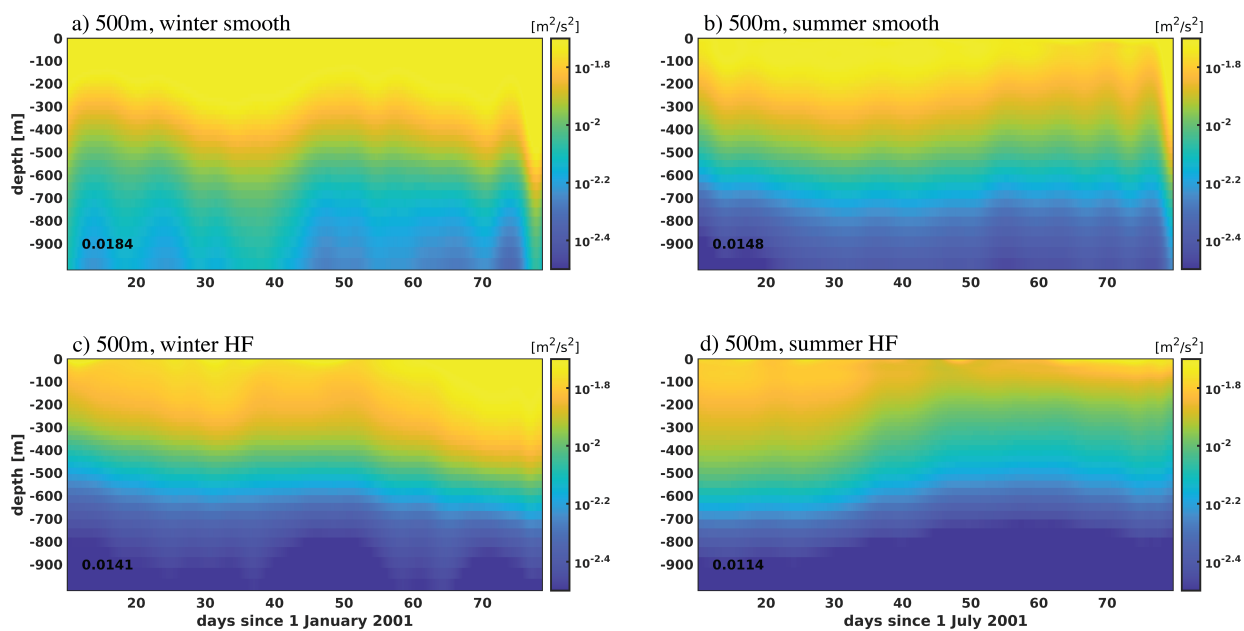
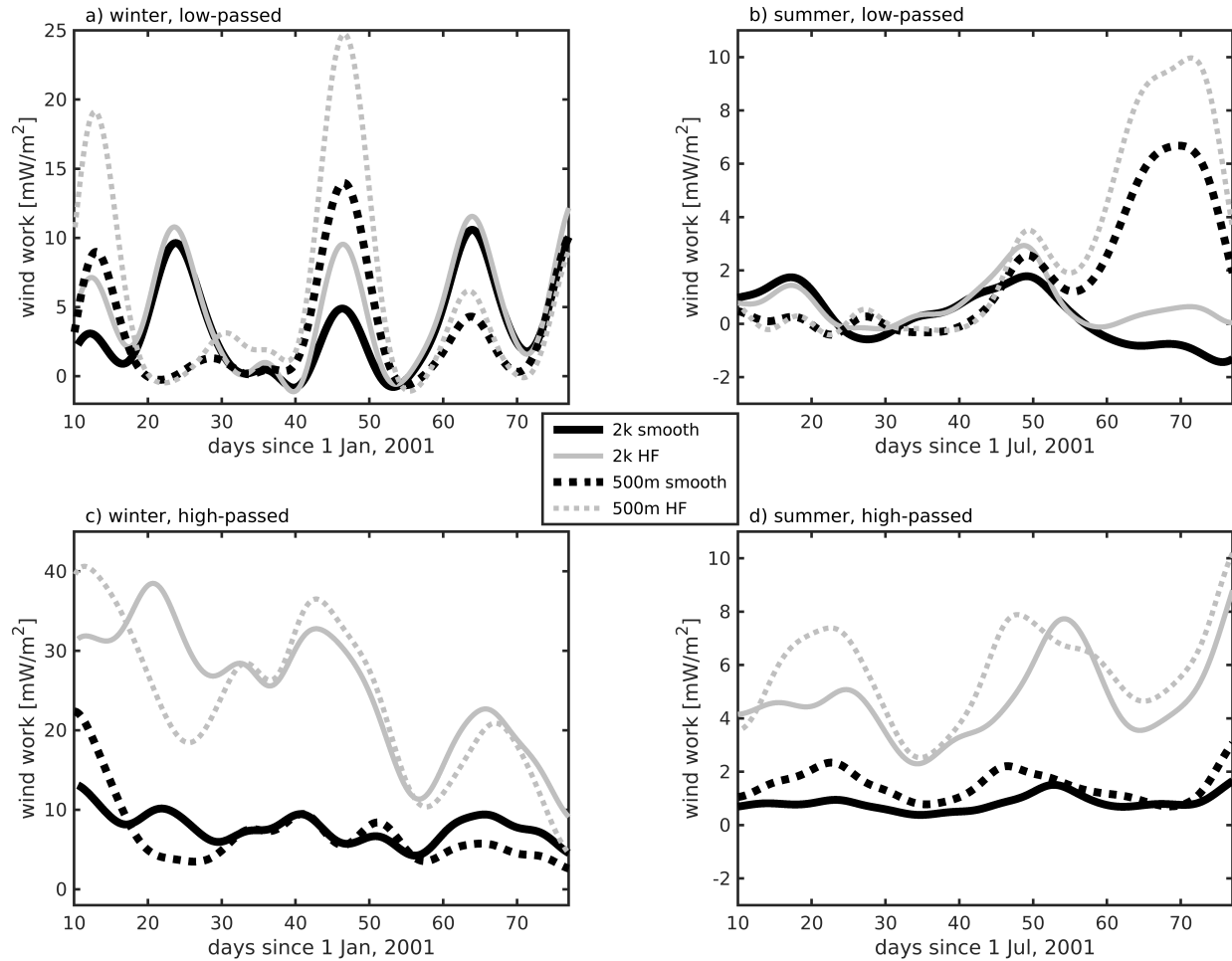Figure S3: Same as Fig. S2 for the 500 m solutions.

Figure S4: Seasonally- and horizontally-averaged a,b) low-passed and c,d) high-passed wind work for the solutions described in the text. Horizontal averages for the 2 km and 500 m solutions are computed over the domains shown in Fig. 1a. A sixth order Butterworth filter with a one week filter width is used for low-passing.
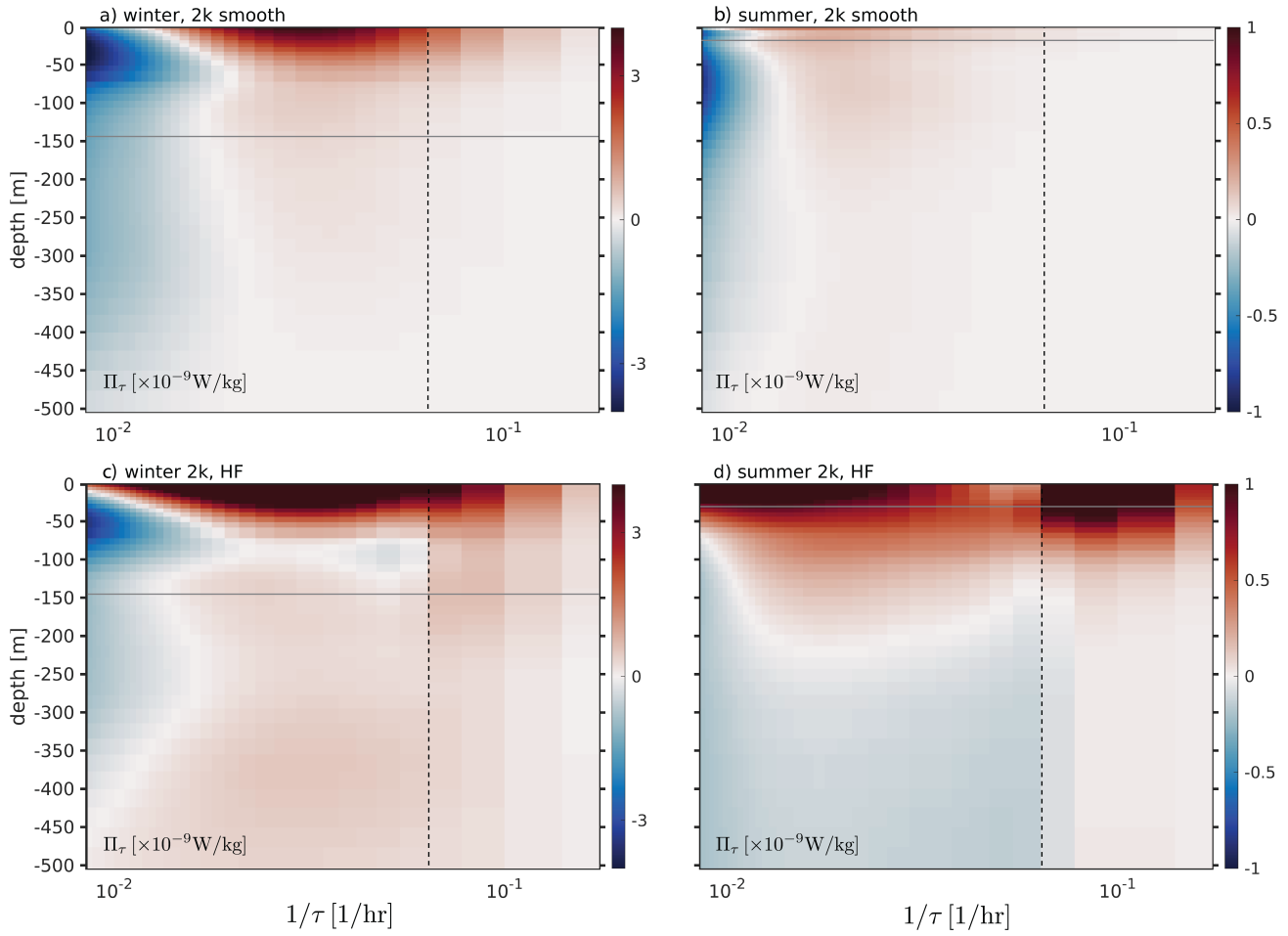
Figure S5: Same as Fig. 3 (panels c-f), but for the 2 km solutions. Horizontal averages are taken over the region occupied by the 500 m grid (Fig. 1a).
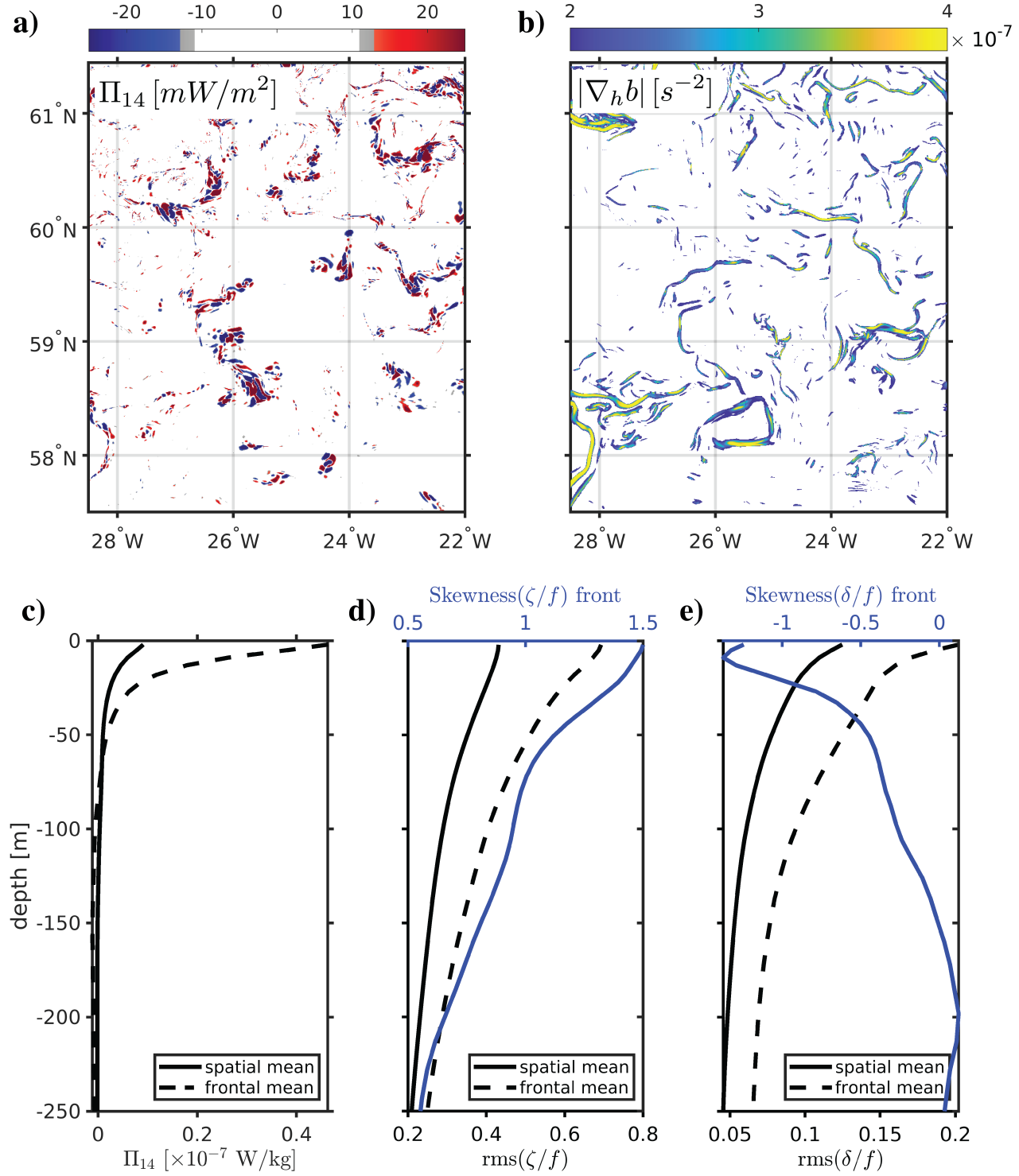
Figure S6: Same as Fig. 4, but for the 500 m smooth solution in winter.

Table S1: Seasonal- and depth-averaged low-passed KE in m^2/s^2 over the top 500 m, where a 6th order Butterworth filter with a 1 week filter width is used for low-passing. The averaging region (2 km grid or 500 m grid) are shown in Fig. 1a.

Grid resolution, averaging region	winter		summer	
	HF	SM	HF	SM
2km, 2km grid	0.0120	0.0156	0.0145	0.0233
2km, 500m grid	0.0112	0.0127	0.0141	0.0167
500m, 500m grid	0.0141	0.0184	0.0114	0.0148